MEASUREMENTS OF ANODE HEAT TRANSFER IN A 1 KW ARCJET

Nicholas T. Tiliakos,* Rodney L. Burton,† and Herman Krier††
University of Illinois at Urbana-Champaign
Urbana, IL 61801

Abstract

A 1 kW hydrazine arcjet thruster has been modified for internal probing of the anode sheath boundary layer with an array of fourteen electrostatic micro-probes flush-mounted into the 2%-thoriated tungsten anode body. Axial and azimuthal distributions of floating potential, anode sheath potential, wall current density, electron number density and electron temperatures have been obtained for arc currents between 7.8 and 10.6 A and propellant flow rates of 40 to 60 mg/s. P/ṁ ranged from 18.8 to 27.4 MJ/kg. Azimuthal symmetry has been verified for all arcjet operating conditions. The sheath is found to be electron-attracting everywhere along the anode, reaching a maximum of 15-18 volts at 1-3 mm downstream of the constrictor. Anode heating is proportional to electron current, multiplied by the sum of electron enthalpy, anode work function, and sheath potential. Most of the current density and resulting anode heat flux is located within 2-4 mm of the constrictor exit, with the location affected more by mass flow rate than by arc current. The axial anode heating distribution accounts for ~18-24% of the total input power.

Nomenclature

I_p	Total probe current [mA]
$I_{e\text{-}sat}$	Electron saturation current [mA]
I	Applied current to arcjet [A]
j_a	Anode current density, [A/cm^2]
j_{th}	Thermal current density [A/cm^2]
k	Boltzmann constant [J/K]
L	Nozzle axial length [mm]
ṁ	Propellant mass flow rate [mg/sec]
m_e	Electron mass [kg]
n_{es}	Electron number density [m^{-3}]
q_e	Anode heat flux by electrons [W/cm^2]
T	Temperature [°K]
V	Voltage [V]
W	2%-Th Tungsten work function [eV]

Greek Symbols

λ_D	Debye length [mm]
ϕ	Potential [V]

Subscripts

arc	Arcjet
a	Anode
e,i	Electron/ion
f	Floating
gas	Plasma-gas flow
p	Probe
s	Pre-sheath/plasma edge.

Introduction

Electrothermal arcjet thrusters are now competitive with chemical propulsion systems for satellite stationkeeping, maneuvering and orbital transfer. To improve arcjet performance further, an understanding is needed of anode heating. The anode energy deposition q_e is mainly due to the electron energy transferred from the arc to the anode, via the current attachment.

This paper describes research conducted to improve the understanding of arc attachment and anode heating processes in the boundary layer of a 1 kW arcjet thruster operating on simulated hydrazine ($N_2 + 2H_2$) propellant.[1,2] A standard 1 kW arcjet was modified to accommodate fourteen micro-probes in the anode body, permitting analysis of anode heat transfer and validation of a numerical model.[3] Two main parameters were varied: arcjet operating current and $N_2 + 2H_2$ propellant flow rate.

Langmuir probes have been employed for plasma diagnostics since the early 1920's, when the method was first developed and implemented.[4] The probe is a wire or sphere inserted into a plasma, biased positive or negative to collect charged particles. The resulting plot of probe current I_p versus probe voltage V_p

*Ph.D. Candidate, Department of Aeronautical and Astronautical Engineering. Present Address: GASL, Inc., Ronkonkoma, N. Y. 11779; Member, AIAA.
†Professor, Department of Aeronautical and Astronautical Engineering, Associate Fellow, AIAA.
††Professor, Department of Mechanical and Industrial Engineering, Fellow, AIAA.

yields information on plasma properties. Electrostatic probes have been used as an anode sheath diagnostic[5,6] and in electric thruster plumes.[7,8] The utility of electrostatic probes is not limited to cylindrical and spherical geometries only. Flush-mounted probes have been used for analyzing the properties in hypersonic flowfields.[9-11]

The achievement of high specific impulse, above 500 seconds for a hydrazine arcjet, requires a specific power $P/\dot{m} > 30$ MJ/kg,[12] resulting in high anode heating rates which can lead to anode failure.[13] Anode heating is determined to a large extent by the physics of current attachment, and to a lesser extent by anode material properties.[14] Therefore, understanding how anode heating is affected by mass flow rate, current and $P/\dot{m}$ is vital to understanding how arcjet design can be improved for more ambitious space mission scenarios.

Experimental Approach

For this study a thruster was fabricated with similar dimensions to a standard 1 kW arcjet thruster,[1,2] and modified to accept electrostatic probes. The major difference from the standard design was elimination of an anode insert and associated seal and implementation of a single-piece thruster body. Use of a monolithic body facilitated modeling of the anode heat transfer, as well as placement of the array of electrostatic micro-probes at various axial and azimuthal locations in the anode wall (Fig. 1).

The arcjet flow passage consisted of a converging cone upstream of the constrictor of 30° half angle, while the diverging section half angle was 20°. The constrictor diameter of 0.63 mm and length 0.25 mm were kept identical to the standard arcjet, as was the axial cathode gap of 0.60 mm ± 0.13 mm. The exit plane diameter was 9.5 mm, providing an area ratio of 225:1.

The arcjet nozzle (anode) was fabricated from 2% thoriated tungsten. The cathode was also fabricated from 2% thoriated tungsten and had a 30° half-angle tip, with a diameter of 4.8 mm at the thruster head.

The probes were numbered to designate the axial distance (mm) from the constrictor exit. Probes 1, 4, 7, and 10 and probes 1', 4', 7' and 10' were at the same axial location, but separated azimuthally by 180° (Fig. 1). The remaining probes were located at 120° and 240° to provide information on current symmetry.

Micro-probes 2-10' were made from 0.43 mm diameter, 99.95% pure tungsten wire, surrounded by an alumina (Al_2O_3) insulator tubing (Fig. 2) with an outer diameter of 0.86 mm and inner diameter of 0.51 mm, inserted into a Type 304 stainless steel support tube, with an inner diameter of 1.22 mm. For probes 1 and 1', 0.17 mm diameter tungsten wire was used, surrounded by an Al_2O_3 tube with an outer diameter of 0.58 mm and inner diameter of 0.20 mm and inserted into a Type 304 stainless steel support tube with an inner diameter of 0.81 mm. The stainless steel tube covers all but the last 2 mm of the probe, and so is not visible in Fig. 2.

To summarize, fourteen micro-probes were located in the anode housing at 10 axial and 4 azimuthal locations downstream of the constrictor. The tungsten probe wire and alumina tubing were held in place with high temperature (2200 K) zirconia adhesive. The wire probe was mounted flush with the anode wall for all experiments. Tungsten was selected for the probe material because of its high melting point, and high work function (4.55 eV),[15] giving low electron emission. Further details regarding probe fabrication techniques are discussed in Ref. 1.

The thruster was operated at a simulated hydrazine flow rate of 40-60 mg/s, with a nominal current of 10 amps, and ~110 volts across the electrodes. The specific power $P/\dot{m}$ ranged from 18.8 to 27.4 MJ/kg.

After each test, all probes were removed from the anode for inspection and re-measurement of their diameter. Data from visibly contaminated or eroded probes was not included in the analysis. The probes were then abrasively cleaned and re-used.

The thruster was mounted inside a 1.5 m^3 vacuum tank, with a background pressure range of 0.1 - 0.2 Torr for flow rates between 40-60 mg/sec. The N_2 + $2H_2$ propellant flow rate was controlled by two Unit Instruments mass flow controllers. A radiation-shielded chromel-alumel type K thermocouple recorded nozzle surface temperature at 9.4 mm from the exit plane.

The plasma properties of floating potential, sheath potential, electron density and temperature at the sheath edge, and anode current density were derived from the probe V-I characteristic,[1] obtained by biasing the probe with a sinusoidal function generator and measuring the probe current I_p with a ~100 Ω current-sensing shunt resistor, recorded on a digital oscilloscope. The function generator frequency was 10 Hz to avoid distortion in the probe V-I characteristic, as well as unwanted voltage drops across the low inductance current sensing resistor. The method of obtaining ϕ_f, ϕ_s, n_{es} and T_{es} from the probe characteristic has been described in detail elsewhere.[1,18]

Experimental Results

Table I summarizes the steady state thruster operating conditions using flush-mounted probes. Results with probes extended up to 0.3 mm into the flow were similar to those of the flush probes.[1]

Table I. Summary of steady state arcjet thruster operating conditions. T_a = Anode Temperature.

$\dot{m}$ [mg/s]	Avg. I_{arc} [A]	Avg. V_{arc}[V]	Power [W]	P/$\dot{m}$ (MJ/kg)	T_a (K)
40	10.6	104	1102	27.4	945
45	9.8	109	1068	23.6	935
50	7.8	121	944	18.8	870
50	8.9	115	1023	20.6	900
50	9.8	112	1098	22.0	910
60	9.9	121	1198	20.0	895

Anode Sheath Potential Distribution

The anode sheath potential ϕ_s is derived from the probe V-I characteristic, and is the negative of the plasma potential ϕ_{pl},[16] where ϕ_{pl} is determined by the intersection of the electron-retarding and electron saturation regions of the V-I curve (Fig. 3).

An expression can be written for anode sheath potential which also provides an estimate of the electron temperature:[17]

$$\phi_s = -\phi_f + \frac{kT_{es}}{e}\left\{\ln(\alpha_c) + \ln\left(0.61\sqrt{\frac{2\pi m_e}{M_i}}\right)\right\}$$

$$\text{where} \quad \alpha_c \equiv \left[1 + \frac{\pi\lambda_D}{2\lambda_{H^+-H_2}}\right]^{-1/2} \qquad (1)$$

The effect of propellant flow rate on the anode sheath potential distribution is shown in Fig. 4. As the propellant flow rate is increased from 40 mg/sec to 60 mg/sec, ϕ_s increases at all probe locations, and the maximum in the ϕ_s axial profile distribution shifts from probe 2 to probe 3.

For flow rates of 40 to 50 mg/sec an absolute maximum exists in the sheath potential at about x = 2 mm. In all cases, ϕ_s decreases monotonically for x $\geq$ 2 mm. Throughout the anode boundary layer ϕ_s is positive, so that the anode sheath is always electron-attracting.

A weighted anode sheath potential is calculated as:

$$\bar{\phi}_s = \frac{\int_0^L j_a(x)\phi_s(x)dA(x)}{I_{arc}} \qquad (2)$$

where x is in mm, $j_a(x)$ is the current density distribution and $\phi_s(x)$ is the anode sheath potential distribution. For the $j_a(x)$ and $\phi_s(x)$ distributions the values for the 0° and 180° probes are averaged to obtain a single data point in Eq. (2).

The weighted anode sheath potential as a function of propellant flow rate exhibits a minimum of 11.3 ± 2.4 V at 50 mg/s and 9.9 A, increasing for $\dot{m} \geq 50$ mg/s.[18] The largest value for $\bar{\phi}_s$, 17 ± 5.1 V, occurs at 60 mg/s and P/$\dot{m}$ of 19.9 MJ/kg. Similarly, for 40 mg/s and 27.4 MJ/kg, $\bar{\phi}_s$ has a low value of 8.1 ± 1.6 V. The results agree in general with Curran et al.,[19] who found an anode fall voltage of O(10-20V).

Electron Number Density

For all flow rates studied, the electron number density n_{es}, which ranges from ~10^{18}-10^{19}m^{-3}, was largest at 1 mm with a secondary peak at 4 mm, and decreased down the nozzle. For all cases, the axial variation of n_{es} varied from 3.5-10x10^{18} m^{-3} at 1 mm, to 7-10 x 10^{17} m^{-3} at 10 mm.

Symmetry in the n_{es} data is reasonable for all flow rates except 45 mg/sec, where the largest n_{es} difference between the 0° and 180° probes was 60%, for probes 1 and 1' only.

Electron Temperature

The electron temperature T_{es} at the pre-sheath/plasma edge, coupled with the ϕ_s and j_a results, is needed to estimate the anode heating q_e. In addition, T_{es} can be used to calculate the scalar electrical conductivity σ and thermal conductivity κ in the anode boundary layer.

The T_{es} distribution is derived from the classical V-I characteristic method, using the inverse slope of the electron-retarding region. However, as shown below, different results were obtained deriving T_{es} from the sheath potentials (Eq. 1).

Electron temperatures derived from the V-I slope method are plotted in Fig. 5 for 3 values of mass flow rate at 9.8 A. For all mass flow rates T_{es} was highest from 1-3 mm, at 30,000 ± 5,000 K, falling to 16,000 ± 4,000 K further from the constrictor.

The symmetry in the T_{es} data for the 0° and 180° probes at 1, 4, 7 and 10 mm is reasonably good, especially at 50 and 60 mg/s. For 45 mg/s the T_{es} data for probes 1, 1' and probes 7, 7' differ by about 32%.

Figure 6 shows experimental electron temperature determined by two different methods for 50 mg/sec and 9.8 A. Higher values of T_{es} are obtained with the "V - I slope" method, and lower values with the "ϕ_f - ϕ_s" method. Both methods agree at 1 mm, and predict T_{es} = 22,000 K. vs. 12,000 K. These results

are compared to a plasmadynamic model[3,18] in which the electron energy equation accounts for inelastic losses to molecular internal energy modes, i.e. rotational, vibrational, excitational, and ionization, through multiplying the electron-molecule collision frequencies by an energy loss factor, δ. The δ = 1200 and 3000 cases in the model predict a maximum electron temperature at x = 2 mm, in agreement with the V - I method. The model and both experimental methods show that the electron temperature decreases for x > 2 mm, and all results predict $T_{es} >> T_g$.

It is difficult to state which method of evaluating T_{es} is better or preferable. The probe V-I characteristic indicates a Maxwellian distribution for the electrons, suggesting that extracting a temperature by this method is appropriate. However, T_{es} based on the plasma potential measurements shows better agreement with the plasmadynamic model. Both data reductions are in rough agreement with measurements by Bufton in the arcjet exit plane,[8] as shown in Fig. 6.

For all propellant flow rates tested, the ratio T_{es}/T_g is much greater than unity in the near-anode region, at all probe locations, since T_e > 10,000 K is required to maintain the electrical conductivity. For a gas temperature of 1400 K, slightly above that of the anode wall, T_{es}/T_g ~ O(7-20). This strongly suggests that a nonequilibrium two-temperature plasma exists in the near anode region of the arcjet.

Current Density

Previous research has shown that the location of maximum j_a is more sensitive to the mass flow rate than to the arcjet operating current.[1,18] The main results for j_a were:

(1) The current density j_a is largest close to the constrictor, and generally decreases monotonically with x, except for 60 mg/s and 9.8 A, where j_a peaked at 3 mm. At the highest specific power tested, 27.4 MJ/kg (40 mg/s, 10.6 A), the largest current density was obtained, 140 ± 57 A/cm^2 at x = 1 mm.

(2) For $\dot{m}$ = 40, 45, and 50 mg/sec the current density is maximum at 1 mm. The current density decreases from 38 ± 11.5 A/cm^2 near the constrictor to ~3.0 ± 0.6 A/cm^2 at 10 mm. At 60 mg/s the location of peak current density shifts to x = 3 mm.

(3) For most of the experimental conditions studied, azimuthal current symmetry is inferred from the j_a data obtained, within experimental error.

(4) Based on parameter studies, $\dot{m}$ affects the j_a distribution more than I_{arc}, with regards to the location of maximum current density.

Anode Heating

The electron energy deposition in the anode sheath was determined as a function of propellant flow rate $\dot{m}$, arcjet operating current I_{arc} and specific power $P/\dot{m}$. The energy deposition into the anode for an electron-attracting sheath is calculated from:[1,20]

$$q_e = j_a \left[5kT_{es} / 2e + \phi_s + W\right] \qquad (3)$$

where the first term in brackets represents the enthalpy of the electrons, the second term is the electron energy gained in traversing the sheath and the last term is the energy gained when the electron recombines with the anode surface. The work function W of the 2% thoriated tungsten anode is taken as 3.7 eV, an average value between that for 2% thoriated and pure tungsten.[15] The plasma properties j_a, n_{es}, and T_{es} vary with propellant flow rate, arcjet operating current and specific energy. For an electron-attracting sheath $j = j_{th}$, where the electron thermal current density is given by the expression $j_{th} = en_{es}(kT_{es}/2\pi m_e)^{1/2}$[ref. 12].

There has been some confusion in the literature over the coefficient of the electron thermal energy term in Eq. 3.[16] For an electron-attracting sheath the electron kinetic energy flux is integrated over an anisotropic Maxwellian distribution, in which the electron perpendicular velocity is shifted by its drift velocity, j/en_{es}, resulting in the 5/2 coefficient in the first term.

The electron heat flux is plotted for three mass flow rates in Fig. 7, showing a similar q_e distribution for 40, 45 and 50 mg/s. Results for these flow rates show a maximum in q_e at 1 mm, with a minor secondary maximum at 4 mm. As with the j_a results, when $\dot{m}$ is increased to 60 mg/s, $(q_e)_{max}$ is displaced downstream to 3 mm, coinciding with the current density result.

Discussion

The effect of varying the arcjet operating current and mass flow rate on electron heat flux is shown in Table II. The location of maximum q_e is at x = 1 mm and q_e generally decreases with increasing distance from the constrictor, i.e. with decreasing j_a. No obvious correlation exists between q_e and any of the operating parameters: $\dot{m}$, I_{arc}, or $P/\dot{m}$. Close to the constrictor the heat flux is 360 to 1420 W/cm^2, depending on operating conditions. This wide range is due to the variation in current density observed at 1 mm. Far from the constrictor at x = 10 mm (the exit plane is at 12.2 mm), q_e generally falls in the range

of 35 - 45 W/cm^2. The anode temperature T_a is an indication of the total heat flux, and correlates with $P/\dot{m}$, but does not correlate well with the measured local heat fluxes.

Table II. Electron Heat Flux vs. Nozzle Position

$\dot{m}$ [mg/s]	Avg. I_{arc} [A]	$P/\dot{m}$ (MJ/kg)	T_a (K)	W/cm^2@ 1 mm	W/cm^2@ 10 mm
40	10.6	27.4	945	1420±600	35±7
45	9.8	23.6	935	480±140	41±8
50	9.8	22.0	910	440±140	45±8
50	8.9	20.6	900	1140±240	42±9
60	9.9	20.0	895	360±150	43±9
50	7.8	18.8	870	1200±350	34±7

If the data at x = 1 mm is ignored, the heat transfer can be represented by a single curve (Fig. 7), for $\dot{m}$ in the range of 40 to 50 mg/s. The decrease in q_e with distance is such that the product $(q_e)dA(x) \sim (q_e)r(x)dx$ is approximately constant, implying that the total heating is evenly distributed with distance.

The variation of q_e with j_a is displayed in Fig. 8, for 50 mg/s and 9.8 A, showing a roughly linear relationship. The slope q_e/j_a has a value of 20 V, implying an electron anode heat transfer of ~200 W.

The total electron energy power deposition to the anode Q_a for an electron-attracting sheath is:

$$Q_a \equiv \int_0^L q_e(x)dA(x) = \int_0^L j_a\left[\frac{5kT_{es}}{2e} + \phi_s + W\right]dA(x) \qquad (4)$$

where $dA(x) = 2\pi r(x)(\cos 20^\circ)^{-1}dx$. For the 0° and 180° probes an average value is used for $q_e(x)$ at x = 1, 4, 7 and 10 mm. The dependence of Q_a on I_{arc} is shown in Fig. 9 for different mass flow rates.

Calculating Q_a from measured values of j_a, T_{es}, and ϕ_s, the electron energy deposition in the anode ranged from 18-24% of total arcjet power. (Table III) These fractional energy values agree well with previous results in experiments with a water-cooled arcjet simulator,[21] for which the percentage of the total power lost to the anode was 20-25 % of the total input power. At 50 mg/s, Q_a averages 212 ± 45 W (20% of input arc power) at 7.8 to 9.8 A. At the lowest mass flow rate, 40 mg/s, Q_a is 20% of the input power. For increasing flow rate at fixed current, Q_a increases to 290 ± 60 W (24% of arc power) at 60 mg/s and 9.9 A. This result is not supported, however, by the anode temperature

Table III. Total Anode Heating

$\dot{m}$ [mg/s]	Avg. I_{arc} [A]	$P/\dot{m}$ (MJ/kg)	T_a (K)	Total Q_a (Watts)	Total Q_a %
40	10.6	27.4	945	225±60	0.20
45	9.8	23.6	935	200±50	0.19
50	9.8	22.0	910	200±40	0.18
50	8.9	20.6	900	230±50	0.22
60	9.9	20.0	895	290±60	0.24
50	7.8	18.8	870	205±45	0.22

measurements, which show a drop in T_a as the Q_a increases from 20% to 24%, suggesting that the propellant may have a cooling effect on the anode.

Conclusions

Internal arcjet diagnostics experiments were conducted using fourteen electrostatic micro-probes flush-mounted in the anode of a 1 kW arcjet thruster operating on simulated hydrazine. It was shown that useful plasma measurements can be obtained with this diagnostic tool in the harsh environment of an arcjet.

Principal conclusions are:

1. The propellant flow rate affects the axial location of maximum sheath potential, current density and electron heating more than the arc current.
2. The location of maxima in the current density, sheath potential, and electron heat flux is just downstream of the constrictor, and is somewhat affected by $\dot{m}$. The peak of the current density and anode heating (W/cm^2) occurs within 2 - 4 mm of the constrictor exit.
3. The electron power deposition into the anode accounts for ~18-24% of the total input power, increasing with mass flow rate.
4. The anode sheath potential is everywhere electron-attracting and accounts for over 50% of the anode heating; a weighted effective anode sheath potential varies between 8-17 V depending on the thruster operating conditions.
5. Contributions to anode heating are from electron enthalpy (~25%), tungsten work function (~25%) and sheath potential (~50%). This indicates that ϕ_s plays the most important role in anode heating.

Acknowledgments

The authors acknowledge support by AFOSR under contracts F49620-92-J-0448 and -0280. Dr. Mitat Birkan is the program monitor. We gratefully acknowledge illuminating discussions with Profs. M. J. Kushner and D. Ruzic; critical assistance from W. Johnson, K. Elam, D. Foley, and J. Frizzell of the University of Illinois; advice and equipment support through T. Haag of NASA Lewis Research Center; and assistance in the laboratory from G. Willmes.

References

[1]Tiliakos, N., *Plasma Properties and Heating at the Anode of a 1 kW Arcjet Using Electrostatic Probes,* Ph. D. Thesis, University of Illinois, Urbana, 1997.

[2]Curran, F. M., and Haag, T. W., "Extended Life and Performance Test of a Low-Power Arcjet," Journal of Spacecraft and Rockets, Vol. 29, No. 4, 1992, pp. 444-452.

[3]Megli, T. W., Lu, J., Krier, H., and Burton, R. L., "Modeling Plasma Processes in 1 kW Hydrazine Arcjet Thrusters," AIAA Paper 96-2965, July, 1996.

[4]Langmuir, I., and Mott-Smith, H. M., *Gen. Elec. Rev.*, 26, 1923, pp. 731; 27, 1924, pp. 449, 583, 616, 726, 810; *Phys. Rev.*, 28, 1926, pp. 727.

[5]Soulas, G. C., and Myers, R. M., "Mechanisms of Anode Power Deposition in a Low Pressure Free Burning Arc," NASA Contractor Report 194442, IEPC Paper 93-194, Sept., 1993.

[6]Gallimore, A. D., Kelly, A. J., and Jahn, R. G., "Anode Power Deposition in Magnetoplasmadynamic Thrusters," *Journal of Propulsion and Power*, Vol. 9, No. 3, May-June 1993, pp. 361-368.

[7]Carney, L. M., and Keith, T. G., "Langmuir Probe Measurements of an Arcjet Exhaust," *Journal of Propulsion and Power*, Vol. 5, No. 3, May-June 1989, pp. 287-293.

[8]Burton, R. L. and Bufton, S. A., "Exit-Plane Electrostatic Probe Measurements of a Low-Power Arcjet." ," *Journal of Propulsion and Power*, Vol. 12, No. 6, Nov.-Dec. 1996, pp. 1099-1106.

[9]Boyer, D. W., and Touryan, K. J., "Experimental and Numerical Studies of Flush Electrostatic Probes in Hypersonic Ionized Flows: I. Experiment," *AIAA Journal*, Vol. 10, No. 12, Dec. 1972, pp. 1667-1674.

[10]Russo, A. J., and Touryan, K. J., "Experimental and Numerical Studies of Flush Electrostatic Probes in Hypersonic Ionized Flows: II. Theory," *AIAA Journal*, Vol. 10, No. 12, Dec. 1972, pp. 1675-1678.

[11]Tseng, R. C., and Talbot, L., "Flat Plate Boundary-Layer Studies in a Partially Ionized Gas," *AIAA J.*, Vol. 9, No. 7, July 1971, pp. 1365-1372.

[12]Butler, G. W. and Cassady, R. J., "Directions for Arcjet Technology Development," *J. of Propulsion and Power*, Vol. 12, No. 6, Nov.-Dec., 1996, pp. 1026-1034.

[13]Lichon, P., and Sankovic, J., "Development and Demonstration of a 600 Second Mission Average Arcjet," *Journal of Propulsion and Power*, Vol. 12, No. 6, Nov.-Dec., 1996, pp. 1018-1025.

[14]Meeks, E., and Capelli, M. A., "A Multi-Fluid Model of Near-Electrode Plasma Behavior," AIAA Paper 93-2103, June 1993.

[15]Goodfellow, K. D., and Polk, J. E., "Experimental Verification of a High-Current Cathode Thermal Model," AIAA Paper 95-3062, July 1995.

[16]Tiliakos, N. T., and Burton, R. L., "Arcjet Anode Sheath Voltage Measurement by Langmuir Probe," *Journal of Propulsion and Power*, Vol. 12, No. 6, Nov.-Dec., 1996, pp. 1174-1176.

[17]Godyak, V. A., and Sternberg, N., *IEEE Trans. Plasma Sci.*, Vol. 18, 1990, pp. 159.

[18]Tiliakos, N. T., Burton, R. L., and Krier, H. "Arcjet Anode Plasma Measurements using Electrostatic Probes," AIAA Paper No. 97-3201, 33rd AIAA/SAE/ASME/ASEE Joint Propulsion Conference, Seattle, WA, July, 1997; submitted *to J. of Propulsion and Power*, July, 1997.

[19]Curran, F. M., Manzella, D. H., and Pencil, E. J., "Performance Characterization of a Segmented Anode Arcjet Thruster," IEPC Paper 90-2582, July 1990.

[20]Oberth, R. C., *Anode Phenomena in High-Current Discharges*, Ph.D. Dissertation, Dept. of Mechanical and Aerospace Engineering, Princeton University, Princeton, N. J., 1970.

[21]Curran, F. M., "An Experimental Study of Energy Loss Mechanisms and Efficiency Considerations in the Low Power dc Arcjet," AIAA Paper No. 85-2017, Sept. 1985.

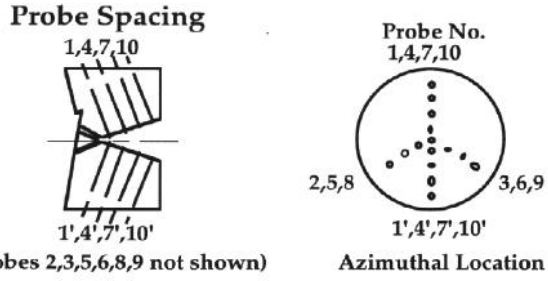

Fig. 1. Schematic of the array of 14 flush-mounted electrostatic micro-probes at millimeter-spaced axial locations. Probes 1, 4, 7, 10 and 1', 4', 7' 10' are used to verify current symmetry.

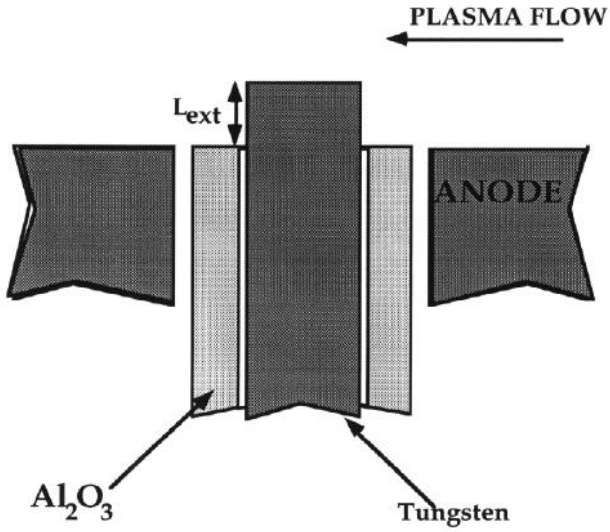

Fig. 2. Shown above is a drawing to scale of the tungsten probe-Al_2O_3 configuration inside the anode. The probe tip extension L_{ext} can be 0.0 - 0.3 mm into the plasma flow, and is set at zero (flush-mounted) for these experiments.

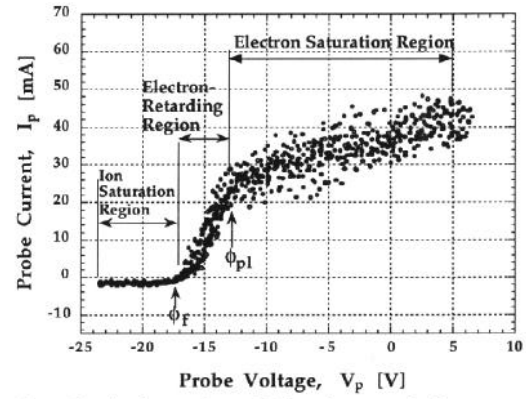

Fig. 3. Typical probe V-I characteristic curve showing regions of interest.

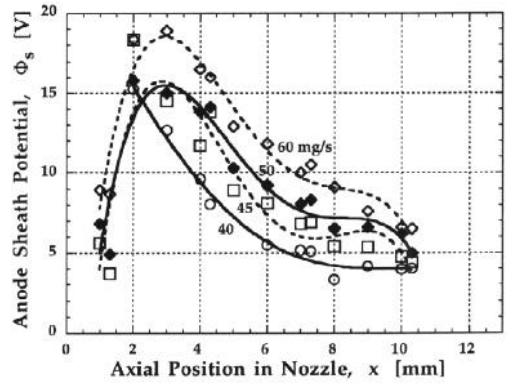

Fig. 4. Sheath potential for 40, 45, 50 and 60 mg/s, at an arc current of ~10 A. In all cases the sheath is electron attracting since $\phi_s > 0$. The error in the sheath potential is ±1 V.

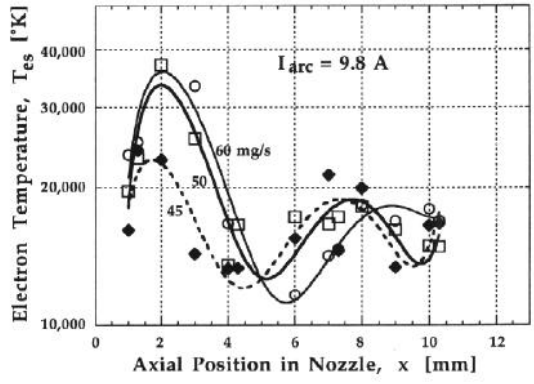

Fig. 5. Electron temperature distributions along the anode for 45, 50, and 60 mg/s and 9.8 A.

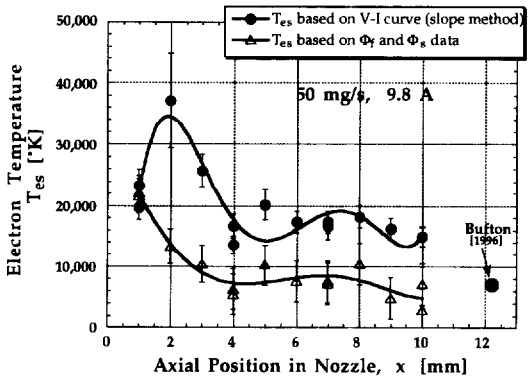

Fig. 6. Determination of T_{es} by the V-I slope and the ϕ_f-ϕ_s methods. The T_{es} data point at the exit plane was obtained from Ref. 8, with an uncertainty of ±15%.

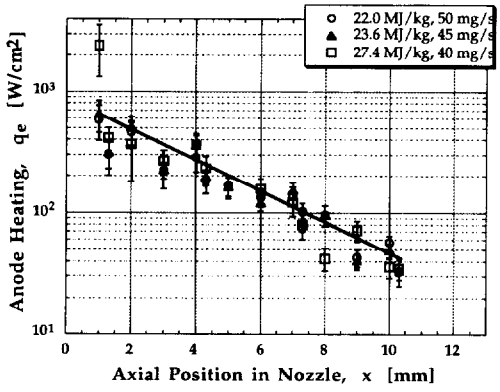

Fig. 7. Distribution of anode heating by electrons q_e for 40, 45, and 50 mg/s, at ~10 A. Error bars are typically ±20%.

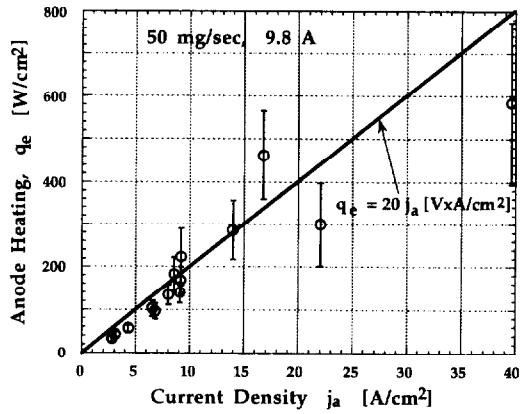

Fig. 8. Anode heating q_e along the anode as a function of current density j_a, for 50 mg/s and 9.8A. The slope is 20 V.

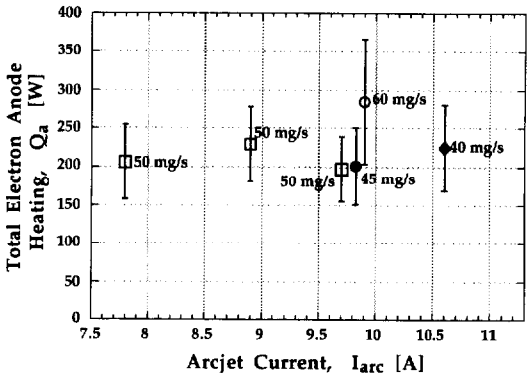

Fig. 9. Total anode heating Q_a as a function of arcjet operating current and $N_2 + 2H_2$ flow rate.